

# Seismic swarms unveil the mechanisms driving shallow slow slip dynamics in the Copiapó ridge, Northern Chile

Jannes Münchmeyer<sup>1,†</sup>, Diego Molina<sup>1,†</sup>, Mathilde Radiguet<sup>1</sup>, David Marsan<sup>1</sup>,  
Juan-Carlos Baez<sup>2</sup>, Francisco Ortega-Culaciati<sup>3</sup>, Andres Tassara<sup>4</sup>, Marcos  
Moreno<sup>5</sup>, Anne Socquet<sup>1</sup>

<sup>1</sup>Univ. Grenoble Alpes, Univ. Savoie Mont Blanc, CNRS, IRD, Univ. Gustave Eiffel, ISTerre, Grenoble, France.

<sup>2</sup>National Seismological Center, University of Chile, Santiago, Chile.

<sup>3</sup>Department of Geophysics, Faculty of Physical and Mathematical Sciences, University of Chile, Santiago, Chile.

<sup>4</sup>Departamento Ciencias de la Tierra, Facultad de Ciencias Químicas, Universidad de Concepción.

<sup>5</sup>Department of Structural and Geotechnical Engineering, Pontificia Universidad Católica de Chile, Santiago, Chile.

<sup>†</sup>These authors contributed equally to this work.

## Key Points:

- We observe a month-long slow slip event ( $M_W = 6.6$ ) in Northern Chile, accompanied by dense, migrating seismic swarm activity.
- The slow slip initiation is likely controlled by migrating fluid overpressure on the segmented interface around a subducted seamount.
- Historic earthquake swarm activity provides evidence for recurrent slow slip with variable magnitude controlled by the interface structure.

**Abstract**

Like earthquakes, slow slip events release elastic energy stored on faults. Yet, the mechanisms behind slow slip instability and its relationship with seismicity are debated. Here, we use a seismo-geodetic deployment to document a shallow slow slip event (SSE) in 2023 on the Chile subduction. We observe dense, migrating seismic swarms accompanying the SSE, comprised of interface activity and upper plate splay faulting. Our observations suggest that the slow slip initiation is driven by structurally-confined fluid overpressure in the fluid-rich surroundings of a subducted seamount. This is consistent with an observed acceleration and expansion of the SSE after a  $M_L = 5.3$  earthquake likely triggering an increase in interface permeability. Historical earthquake swarms highlight the persistent structural control and recurrent nature of such slow slip events. Our observations provide insight into the interactions between slow slip and seismicity, suggesting they are controlled by creep on a fluid-infiltrated fault with fractally distributed asperities.

**Plain Language Summary**

Subduction zones continuously accumulate stress from tectonic plate movement. Part of this stress is released in earthquakes, but another part is released through transient deformations, so-called slow slip events (SSEs). SSEs lead to the same motion on the plate interface as regular earthquakes, but happen over a much longer timeframe of weeks to months. SSEs do not cause ground shaking, but they are important to understand the mechanisms leading to major earthquakes. Here, we report on the first shallow SSE observed in Northern Chile, in the area of the subducted Copiapó ridge. We combine geodetic observations with a high-resolution earthquake catalog to study the mechanisms of slow slip. We find dense earthquake swarms, migrating together with the slow slip. Our findings suggest that the SSE and swarms are both caused by migrating fluid pulses traveling through a fluid-rich plate interface. The fluid-rich environment results from a subducted seamount on the Copiapó ridge. The partition of stress release into slow slip and micro-earthquakes can be explained with a segmentation of the plate interface into an aseismic medium with embedded seismic patches. Our results provide new insight into the mechanisms of SSE initiation and the interplay between slow slip and regular seismicity.

**1 Introduction**

Subduction plate interfaces continuously accumulate stress due to tectonic forcing. This stress is released through earthquakes or slow slip events (SSEs), which last from days to months and typically do not emit strong seismic waves (Ide et al., 2007; Take-mura et al., 2023; Delahaye et al., 2009). The physical parameters that determine whether a rupture is slow or fast, and the mechanisms driving slow slip instability are still debated (Nielsen, 2017; Ide et al., 2007; Obara & Kato, 2016; Kato & Ben-Zion, 2021; Molina-Ormazabal et al., 2023). Furthermore, although slow slip events have been involved in the triggering (Radiguet et al., 2016; Voss et al., 2018; Uchida et al., 2016), nucleation (Obara & Kato, 2016; Nishikawa & Ide, 2018; Itoh et al., 2023) or arrest (Uchida & Matsuzawa, 2013; Rolandone et al., 2018; Itoh et al., 2023) of large earthquakes, how slow slip is related to seismic rupture is still poorly understood.

Several studies suggest that the megathrust interface is segmented into slow and fast slipping regions (Kaneko et al., 2010; Molina et al., 2021; Molina-Ormazabal et al., 2023) down to small-scale (Seno, 2003; Behr et al., 2021; Lavier et al., 2021; Yabe & Ide, 2014). These segments differ in terms of lithology, geometry, stress heterogeneity, and fluid availability (Manga et al., 2012; Gosselin et al., 2020; Nakajima & Uchida, 2018; Warren-Smith et al., 2019). While the origin of this segmentation is not fully understood, a commonly proposed mechanism is a structural control by subducted oceanic structures,

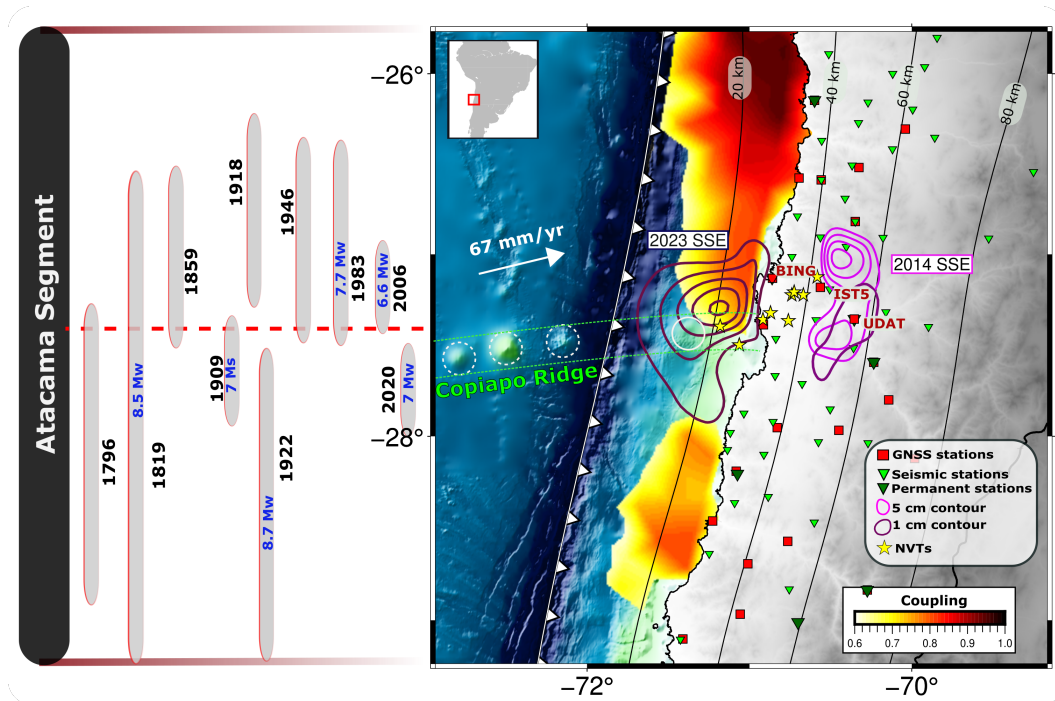


**Figure 1.** Overview of the study region with the Nazca plate subducting below the South American plate. Copiapó ridge highlighted by bathymetry map. Background warm colors show the locking degree (González-Vidal et al., 2023). Dark green triangles denote permanent seismic stations, light green triangles temporary seismic stations, red squares GNSS stations. Colored contours show the SSE in 2014 (pink, (Klein et al., 2018)) and 2023 (maroon, this paper). Yellow stars indicate non-volcanic tremor on 20/09/2019 (Pastén-Araya et al., 2022). On the left, the along strike extent of historic earthquakes is shown (Ruiz & Madariaga, 2018; Vigny et al., 2024).

such as seamounts (Singh et al., 2011; Barnes et al., 2020; Yáñez-Cuadra et al., 2022; González-Vidal et al., 2023; Contreras-Reyes & Carrizo, 2011). To keep the rupture slow, those segments need to be controlled by mechanisms preventing the acceleration into fast ruptures while maintaining slow ruptures. Potential mechanisms to initiate and maintain a slow rupture are fluid pressure migrations, frictional heating, or a control through velocity strengthening friction (Warren-Smith et al., 2019; Wang & Barbot, 2023). Yet, monitoring these processes and the fine-scale segmentation directly has proven challenging due to insufficient resolution.

Here, we use surface deformation and swarm seismicity associated with an SSE in 2023 in the subduction Copiapó ridge, Northern Chile, to investigate the processes and structures driving the SSE initiation and propagation. Between November 2020 and February 2024, the Copiapó ridge has been monitored with a dense network of GNSS (Socquet et al., 2023) and seismic stations. We use the high-resolution earthquake catalog by Münchmeyer et al. (in prep) inferred from the seismic records using deep learning techniques. The catalog contains very precise event hypocenter estimates: in the SSE area, typical relative errors for events at an interevent distance of 500 m are below 50 m and for events at a distance of 5 km below 100 m (Münchmeyer et al., in prep) (Figures S1, S2). These observations allow to mitigate the observational gap obstructing our understanding of the mechanisms driving the slow slip instability and its interactions with seismicity. We are able to monitor with unprecedented detail how the SSE initiated, and what phenomenon triggered the SSE expansion and propagation. Our study sheds light on the role of structural complexities in trapping pressurized fluids, and on the interplay between slow slip, seismicity, and fluid pressure migrations.

## 2 The subducted Copiapó ridge and the 2023 shallow SSE

At the latitude of Copiapó, an oceanic ridge enters into subduction, as marked by a series of aligned seamounts, corresponding to bathymetric anomalies of 2 to 3 km compared to the surrounding seafloor (Maksymowicz et al., 2024) (Figure 1). Above the megathrust, a local positive topographic anomaly is most likely the surface expression of a subducted seamount (Figure 1), as already shown in other settings (Bangs et al., 2023). The megathrust around the subducted Copiapó ridge is characterized by a low locking degree (Figure 1) (González-Vidal et al., 2023) and has repeatedly served as a barrier to seismic ruptures (Comte et al., 2002; Ruiz & Madariaga, 2018; Vigny et al., 2024). A large earthquake is pending in this region, as adjacent locked patches have not been ruptured by a large earthquake ( $M_w > 8$ ) since at least 1922 (Kanamori et al., 2019; González-Vidal et al., 2023; Vigny et al., 2024). The region is known to host seismic swarms with reports dating back to 1973 (Comte et al., 2002; Ojeda et al., 2023; Marsan et al., 2023). Previous studies have reported deep SSEs (40 to 60 km) (Klein et al., 2018, 2022) with a duration of  $\sim 1.5$  years and a 5 year return period, and rare occurrences of non-volcanic tremors (Pastén-Araya et al., 2022), but no shallow slow slip had previously been observed.

In September 2023, we recorded a month-long transient motion on 18 GNSS stations between 26.1°S and 28.4°S with surface displacements up to 8 mm (Figures S3, S4). By inverting the slip on a dislocation in an elastic medium, we infer a shallow SSE in the Copiapó ridge with geodetic  $M_w = 6.6$  (Figures 2, 3, Texts S1-S3). The associated slip patch extends over  $\sim 100$  km along strike between 25 and 35 km depths. The peak slip of  $\sim 5$  cm is located on the edge of the inferred subducted seamount. The 2023 SSE is located updip of the deep SSEs with a band of interface seismicity separating their slip patches (Klein et al., 2018, 2022; Münchmeyer et al., in prep). Although our inversion revealed a small, deep, secondary slip patch with peak slip below 2 cm in the area of the deep 2020 SSE (Figure S3), it is unclear if this results from actual slip or insufficient resolution. The SSE starts around September 1st, increases in slip rate in the second half of September, before arresting in early October (Figure 3). Individual slip inversions for

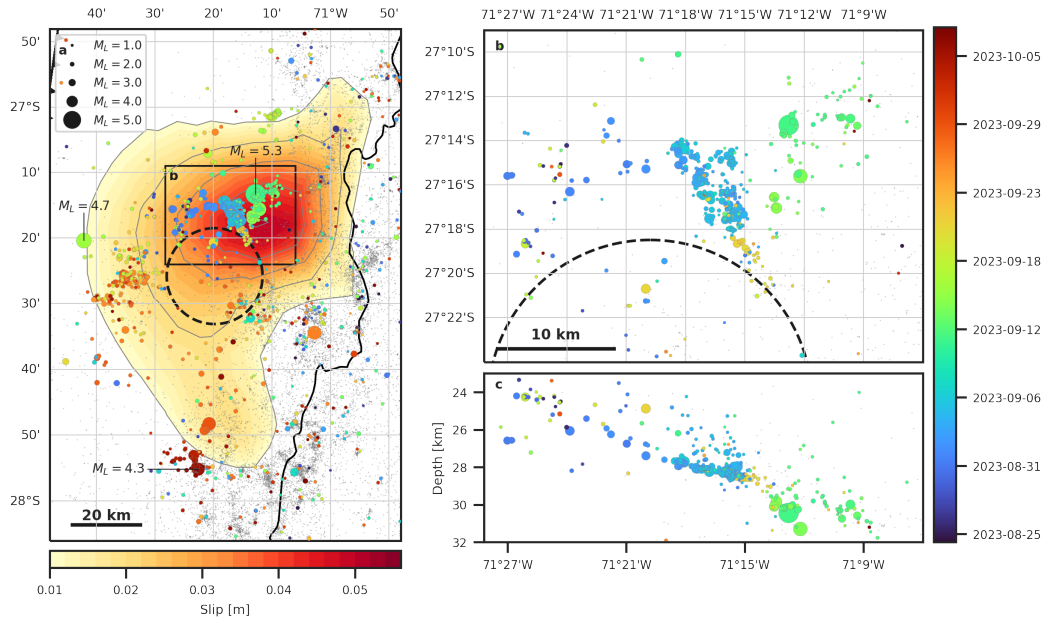


**Figure 2.** **a** Slip distribution and seismicity during the 2023 slow slip event. The slip distribution is shown in yellow to red with additional grey 1 cm contours. Earthquakes during the time period are colored by time in the sequence and scaled by magnitude. For reference, all seismicity cataloged between 11/2020 and 02/2024 is shown as grey dots. **b** Zoom in on the onset cluster. **c** Cross section of the events in **b** along longitude. The black dashed circle in **a** and **b** indicates the approximate position of the subducted seamount inferred from bathymetric features and gravity data.

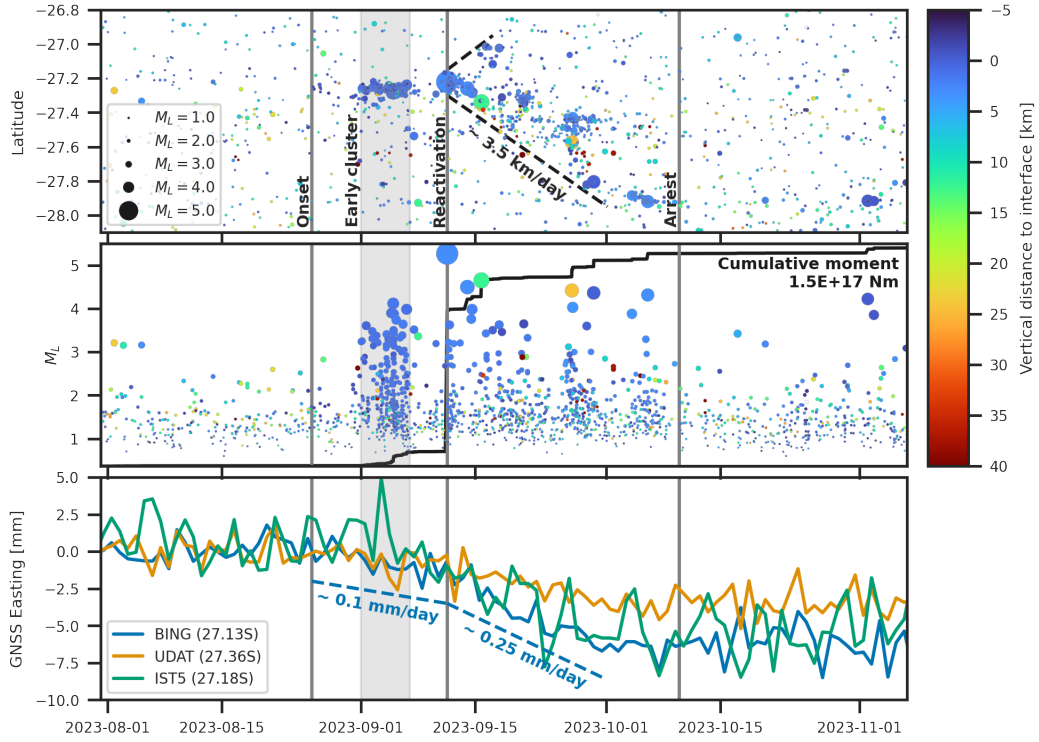


**Figure 3.** Temporal development of latitude distribution, magnitudes, and detrended GNSS series. The top two plots include all events shown in Figure 2a. The black line in the magnitude plot shows the total cumulative seismic moment release. GNSS time series have been selected for stations close to the main slip patch of the SSE. We highlight the approximate GNSS velocities at the station BING with blue dashed lines.

the early ( $M_w = 6.16$ , until 10/09, Figure S3a) and late periods ( $M_w = 6.52$ , Figure S3b) of the SSE indicate localized slip around the edge of the subducted seamount in the first phase and a substantially larger slip with bidirectional expansion afterwards.

The SSE is accompanied by seismic swarm activity with complex migration patterns (Figures 2, 3). The cumulative seismic moment release is  $M_w = 5.4$ , only about 1.6 % of the geodetic moment release. Swarm seismicity starts on August 26 within a well-confined, low-magnitude cluster (total  $M_w < 3.0$ ) on the northern edge of a subducted seamount. On September 1st a vigorous swarm is activated downdip, in the area of highest geodetic slip. After a five-day quiescence, an interface earthquake ( $M_L = 5.3$ ) marks the acceleration of the geodetic displacement. It also marks the onset of a large-scale, bilateral migration of the seismicity at a rate of  $\sim 3.5$  km/day (Figure 3), a typical migration rate of month-long SSEs (Danré et al., 2022, 2024). The short northward migration terminates after 20 km with three magnitude 3.5 earthquakes within 2 days. The southward migration terminates around  $27.9^\circ\text{S}$  with the last large event ( $M_L = 4.3$ ) on October 6th. The migration activates several seismicity clusters surrounding the seamount, among which the largest occurs updip of the inferred slip area, including one  $M_L = 4.7$  event. Within the area of the seamount, only few isolated events occur (Figure 2), yet these fit the surrounding seismic migration patterns.

The seismo-geodetic joint monitoring suggests two different phases during the SSE (Figure 3). In the initiation phase, up to the  $M_L = 5.3$  event and the geodetic acceleration, seismicity and slip collocate in a small area. In the second phase, the slow slip and the seismicity are migrating over larger distances at a constant velocity, with the seismic activity primarily surrounding the main slip patch. Such two-phase SSE behaviour has previously been observed, for example, in Cascadia (Gomberg et al., 2016; Itoh et al., 2022). To understand the SSE’s initiation mechanisms, we now focus on the seismic activity before the expansion of geodetic slip.

### 3 Seismic swarms outlining the SSE initiation

The full initiation sequence of the SSE occurs along the northern flank of the subducted seamount (Figure 2 b,c). It commences with an initial weak burst of seismicity on August 26th (blue in Figure S5). From September 1st to 6th a second cluster is activated downdip (cyan), confined to a narrow area of approximately 10 km by 3 km. Within this swarm, a double migration occurs: the main activity migrates southwards with a slowly decaying rate between 2 and 5 km/day. It is interspersed with bursts migrating with velocities above 15 km/day (Figure S6). Such double migrations and interactions between slow slip and seismicity are indicative of pressure pulses triggering asperities on creeping faults infiltrated by fluid (Dublanche & De Barros, 2021).

This second swarm is clearly delineated downdip by a gap in the seismicity. Activity beyond this gap only occurs after a 5 day quiescence and initiates with an  $M_L = 5.3$  earthquake on September 11th. Within the first two days, the aftershocks of this event (green) expand within an area of around  $75 \text{ km}^2$  with an expansion rate typical for afterslip (Perfettini et al., 2018) (Figure S7). The three onset clusters show qualitatively different magnitude distributions (Figure S5). The third cluster, containing the largest event, show approximately Gutenberg-Richter distributions. In contrast, the second cluster, with by far the highest event count, shows a clear scale break around  $M_L = 3.2$ . This scale break suggests spatially confined ruptures, for example, due to limited size of the seismic asperities (Seno, 2003; Behr et al., 2021).

Within this early sequence, almost all events locate on the narrow plate interface (Figure S6). In addition, we are able to resolve earthquakes on splay fractures trending westward in the upper plate. The seismic activity shows that the splay fractures extend over several kilometers. Timing of upper plate seismicity coincides with the activation

of interface seismicity and is most active above the second cluster (cyan in Figure S5). This activity of splay fractures might be indicating the drainage of fluid overpressure from the interface (Chesley et al., 2021; Perez-Silva et al., 2023).

#### 4 Revisiting historic swarm activity

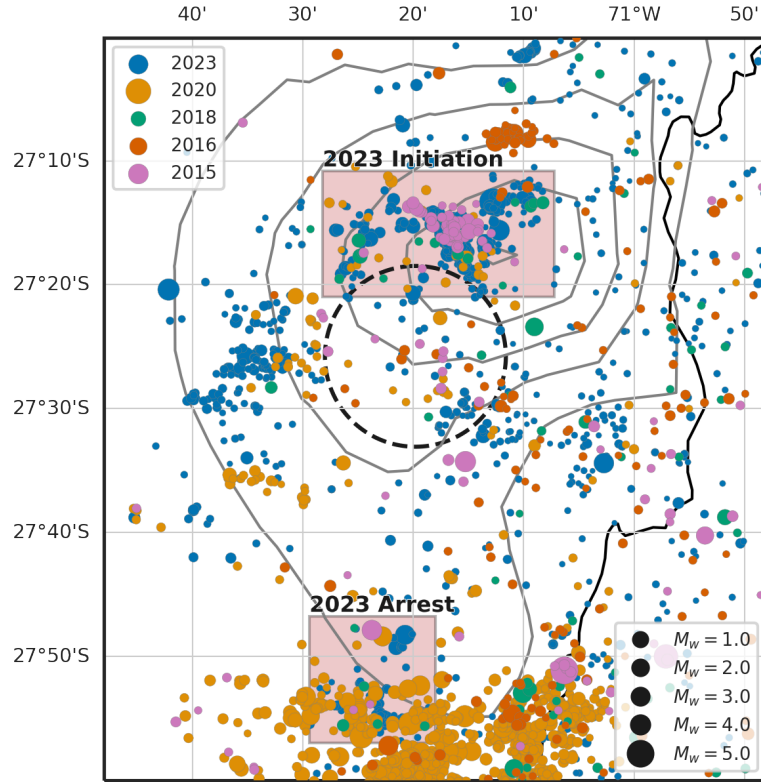


**Figure 4.** Zoom in on the central part of the 2015, 2016, 2018, 2020 and 2023 swarms using catalogs from Münchmeyer et al. (in prep). The black circle highlights the approximate location of the subducted seamount. Grey lines show the 1 cm slip contours of the 2023 SSE. All swarms have been located with the same 3D seismic velocity model. The 2015 to 2020 swarms use similar station coverage, consisting of permanent seismic networks, while for the 2023 swarm a collection of much denser temporary networks was used. Therefore, catalog completeness and location accuracy are best for the 2023 swarm. The 2015 to 2020 swarms have been jointly relocated using GrowClust3D, the 2023 model individually.

In order to investigate whether such events are recurrent and if any repetitive pattern is found, we compare the swarm activity in 2023 to nine historic swarms around the Copiapó ridge. These swarms encompass newly detected sequences and known swarms using four seismic catalogs (Figures 4, S6) (Comte et al., 2002; Ojeda et al., 2023; Marsan et al., 2023). Due to limited detection capabilities, especially prior to 2014, we likely miss additional swarms in between the early swarms. The five swarms with sufficient data (2015, 2016, 2018, 2020, 2023) have been located using a common 3D velocity model. These swarms consistently activate the same interface patches, in particular, in the initiation phase around the seamount and in the arrest region of the 2023 SSE (Figure 4). The active patches match at least down to the kilometer scale, similar to the location uncer-

tainties of the longer-term catalog used for the swarms from 2015 to 2020. This suggests that the location of the swarm seismicity is controlled by persistent interface structures that are repeatedly activated. This observation is consistent with the previous observation that the 2023 initial swarm is structurally confined.

While geodetic records are insufficient to detect potential SSEs, several indicators point at slow slip associated with the swarm activity. Most prominently, all swarms exhibit migration patterns (Figure S8). This is particularly evident for the 1973 swarm (northward migration) and the 2006 swarm (bilateral). Furthermore, for the 2006 sequence, one continuous GNSS station running during the swarm detected seaward motion of the upper plate, consistent with a shallow SSE (Ojeda et al., 2023). For the 1973 event, moment tensor solutions show that the events features thrust mechanisms, indicating that the seismicity is mostly located on the subduction interface (Comte et al., 2002). Notably, the region shows almost no seismic activity in between the seismic swarms. In combination with the observed migration patterns, this suggests that swarm seismicity is caused by outside drivers, such as recurrent SSEs.

The detected swarms vary in seismic moment by almost three orders of magnitude. As geodetic moment typically scales with seismic moment, this suggest that the region possibly hosts repeated SSEs with highly varying moment release (Nishikawa & Ide, 2018; Passarelli et al., 2021; Wang & Barbot, 2023). Given this observations, it seems possible that the low locking in this area is not the result of continuous creep, but that the slip pattern is highly intermittent, with episodes of large slip detectable as SSEs with accompanying seismic swarms. Such intermittence on short time-scales is not resolvable in on-shore geodetic data, and will require offshore deployments to verify.

## 5 The structure of the subduction interface

Based on our observations, we infer a schematic model of the SSE area (Figure 5). The high resolution of the earthquake catalog shows that the subduction interface is only seismically active on small patches (Figure 5 inset), each of them extending up to 50 m vertically and up to 2 km horizontally. We observe rapid migrations within these patches. The individual patches are disconnected from each other and distributed within a thin, 3D fault interface volume of less than 250 m thickness, overall forming the subduction interface on a macroscopic scale (Figure S6 right). This is consistent with estimates of the interface thickness in other subduction zones (Chalumeau et al., 2024). The patches show a fractal behaviour from a length scale of 5 km down to the location uncertainty around 40 m, meaning that the seismic patches cluster and are themselves subdivided into smaller seismic patches (Figure 5 inset, Figure S1). Our comparison to historic swarms shows that this segmentation into seismic and aseismic patches is stable at least on the decade scale. As the total seismic moment is insufficient to accommodate the geodetic moment, the seismic patches need to be embedded within a slowly deforming matrix (Seno, 2003; Perfettini et al., 2018; Behr et al., 2021; Lavier et al., 2021). This observation is consistent with geological observations of fossil subduction interfaces, a shear zone with frictional lenses embedded in a viscous and fluid-rich matrix (Behr et al., 2021).

To explain the episodic, swarm-type seismic behaviour and the transient slow deformation, we suggest a central role of pressure pulses migrating on a fluid-rich interface (Figure 5 I-III). Such recurrent fluid pressure increases are evidenced by swarm seismicity, the characteristic double-migration patterns (Figure S6) (Dublanche & De Barros, 2021), the activation of splay fractures for fluid pressure drainage (Figure 5 cross-section) (Fasola et al., 2019; Chesley et al., 2021), and the typical migration velocities (Figure 3) (Danré et al., 2022). Furthermore, the seismic quiescence between September 6th and 11th suggests the existence of a structural permeability seal (Figure 5 IV), (Manga et al., 2012; Gosselin et al., 2020). Before its rupture, the overpressured fluids, structurally confined by the seal, lower the effective normal stress and thereby trigger the most active seis-

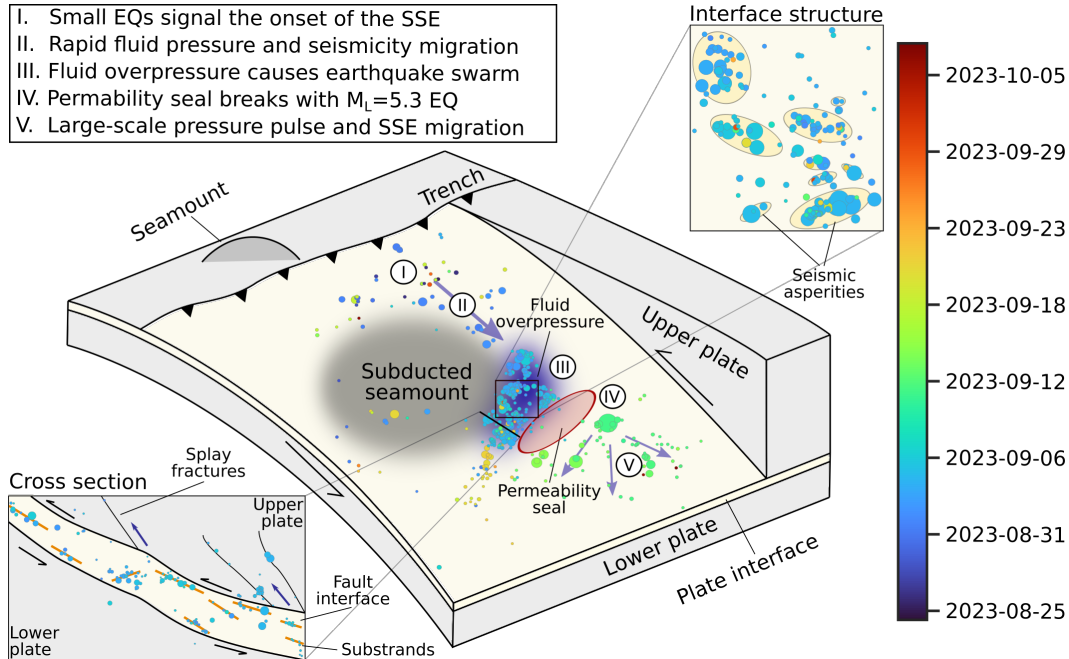


**Figure 5.** Schematic overview of the SSE initiation sequence and its drivers. Each earthquake is represented by a dot colored according to the time within the sequence. Blue arrows show fluid pressure migrations. The insets show a cross section of the fault interface (bottom left) and the interface structure in bird's eye perspective (top right).

munity swarm in the sequence. This fluid overpressure infiltrating the size-constrained asperities explains the scale-break observed in the magnitude distribution of the onset cluster (Figure S5). Once shear stress on the asperities is released, the cluster goes dormant, even though fluid pressure stays high. During this cluster and the subsequent quiescence, the aseismic slip remains confined to the initiation area. Only once the permeability seal is broken, as marked by the  $M_L = 5.3$  event, the fluid pressure pulse can migrate further along the interface, triggering the expansion of slow slip on the interface together with the large-scale seismic migration (Figure 5 V). During that propagation stage, the seismicity is produced by the rupture of the seismic asperities as a response to their transient loading by the propagation of the slow slip front. This is again compliant with a model of seismic asperities embedded in a slowly creeping matrix (Yabe & Ide, 2014). The propagation of the slow slip is likely arrested by stronger seismic asperities (Yabe & Ide, 2014), as shown by the peripheral location of the seismic swarms with the largest magnitudes compared to the area slipping slowly and inferred by GPS (Figure 2).

The initiation of the slow slip event, as imaged by the seismic swarm activity, occurs along the northern flank of a subducted seamount (Figure 2). Abundant evidence suggests that subducted ridges stay intact after subduction, leading to zones of low coupling in its wake, and enhance increased normal stress on its leading edge and weakening of the surrounding medium through fracturing (Singh et al., 2011; Barnes et al., 2020; Contreras-Reyes & Carrizo, 2011; Sun et al., 2020). Furthermore, seamount flanks are typically observed to feature overpressurized sediments, caused by the subducting topography and have been shown to supply fluids to the interface (Shaddox & Schwartz, 2019; Gase et al., 2023; Bangs et al., 2023; Chesley et al., 2021; Sun et al., 2020). We hypothesise that this high fluid pressure on the interface enables the migrations of pres-

sure pulses as described above (Cruz-Atienza et al., 2018). Further evidence for a fluid-rich environment is provided by tomographic studies, showing high  $v_p/v_s$  ratios in this region (Pastén-Araya et al., 2022). Notably, while in our observation the highest activity occurs on the northern flank of the seamount, we see further swarms on its western and south-eastern edges, suggesting similar interactions of interface segmentation and fluid overpressure. Combining these aspects, the seamount together with the inherited oceanic fractures likely controls the interface segmentation and creates a fluid-rich environment, enabling seismic swarm activity and slow deformation.

A few peculiarities should be noted regarding the swarm behaviour and its relation to fluid pressure: the downdip migration, the roughly constant migration velocity, and the high value of the migration velocity. All three aspects would be unexpected for fluid diffusion, but are fully compatible with pressure pulses on a fluid-rich interface during slow slip (Cruz-Atienza et al., 2018; Perez-Silva et al., 2023; Farge et al., 2021, 2023). This is caused by transient changes in permeability, due to changes in effective pressure and dilatancy from the slow slip, and by anisotropy of the permeability (Kawano et al., 2011). We note that this is not the only interaction mode of slow slip with seismic swarms. Alternative modes are intraplate swarms in the subducting plate, related to the fluid supply to the interface (Nishikawa et al., 2021), and swarms on upper plate faults caused by fluid drainage (Fasola et al., 2019).

The micro-structures and pressure pulse migrations define the macro-structure of the subduction megathrust and its seismic potential. Differential stresses built up by repeated SSEs increase the likelihood of triggering large earthquakes in adjacent segments (Radiguet et al., 2016; Obara & Kato, 2016). At the same time, the predominantly aseismic interface acts as an energy sink for seismic rupture propagation (Kaneko et al., 2010; Molina et al., 2021), explaining the barrier behaviour of this region (Ruiz & Madariaga, 2018; Vigny et al., 2024). The seismic patches encircling the seamount indicate that, although the Copiapó ridge generally acts as a barrier, it might still break during a megathrust rupture with sufficient along-dip extent (Rice & Ben-Zion, 1996; Yáñez-Cuadra et al., 2022).

## 6 Conclusion

Our findings combine dense seismo-geodetic observations to study the 2023 Copiapó SSE and its seismic swarm activities. Using a high-resolution catalogue, we gain a detailed view of the mechanisms of shallow slow slip and the subduction interface structure. Our observations suggest that the interplay of a fine-scale interface segmentation with migrating fluid pressure pulses controls both slow slip and the associated swarm seismicity. Notably, our study describes the initiation phase of a slow slip event with unprecedented detail. The slow slip instability initiates with a structurally controlled seismic swarm driven by pressurized fluids, that eventually triggers the acceleration and propagation of the slow slip after the rupture of a permeability seal. The link between slow slip and seismicity significantly differs between the initiation and the propagation phases of the SSE, indicating that the driving mechanisms evolve from the slow slip initiation to its propagation. Our results also provide a detailed perspective on the functioning of a seismic barrier, and thereby the understanding of fast and slow megathrust earthquakes.

## Open Research Section

The seismicity catalog and geodetic data will be made public upon acceptance of the manuscript.

## Acknowledgments

We thank everyone involved in the deployment of the seismic and geodetic networks and the data management. The computations presented in this paper were performed using the GRICAD infrastructure (<https://gricad.univ-grenoble-alpes.fr>), which is supported by Grenoble research communities. This work has been partially funded by the European Union under the ERC CoG 865963 DEEP-trigger and the grant agreement n°101104996 (“DECODE”). Views and opinions expressed are however those of the authors only and do not necessarily reflect those of the European Union or REA. Neither the European Union nor the granting authority can be held responsible for them. D.M.’s salary was covered by a grant from CNES. J-C.B., F.O-C. and M.M. acknowledge funding from ANID PIA-ACT192169 Anillo PRECURSOR project. F.O-C. acknowledge support from FONDECYT 1231684 ANID project. M.M. acknowledge support from FONDECYT 1221507 ANID project. J-C-B. acknowledge support from FONDECYT 1240501 ANID project. Stations from the 9C network were funded by CNRS-Tellus “COP2020: SlowSlip Trigger” and ANR-S5 (ANR-19-CE31-0003) projects.

## References

- Bangs, N. L., Morgan, J. K., Bell, R. E., Han, S., Arai, R., Kodaira, S., . . . Fry, B. (2023, June). Slow slip along the Hikurangi margin linked to fluid-rich sediments trailing subducting seamounts. *Nature Geoscience*, *16*(6), 505–512. doi: 10.1038/s41561-023-01186-3
- Barnes, P. M., Wallace, L. M., Saffer, D. M., Bell, R. E., Underwood, M. B., Fagereng, A., . . . others (2020). Slow slip source characterized by lithological and geometric heterogeneity. *Science Advances*, *6*(13), eaay3314.
- Behr, W. M., Gerya, T. V., Cannizzaro, C., & Blass, R. (2021). Transient Slow Slip Characteristics of Frictional-Viscous Subduction Megathrust Shear Zones. *AGU Advances*, *2*(3), e2021AV000416. doi: 10.1029/2021AV000416
- Bertiger, W., Bar-Sever, Y., Dorsey, A., Haines, B., Harvey, N., Hemberger, D., . . . others (2020). Gipsyx/rtgx, a new tool set for space geodetic operations and research. *Advances in space research*, *66*(3), 469–489.
- Chalumeau, C., Agurto-Detzel, H., Rietbrock, A., Frietsch, M., Oncken, O., Segovia, M., & Galve, A. (2024, April). Seismological evidence for a multifault network at the subduction interface. *Nature*, *628*(8008), 558–562. doi: 10.1038/s41586-024-07245-y
- Chesley, C., Naif, S., Key, K., & Bassett, D. (2021, July). Fluid-rich subducting topography generates anomalous forearc porosity. *Nature*, *595*(7866), 255–260. doi: 10.1038/s41586-021-03619-8
- Comte, D., Haessler, H., Dorbath, L., Pardo, M., Monfret, T., Lavenu, A., . . . Hello, Y. (2002, September). Seismicity and stress distribution in the Copiapo, northern Chile subduction zone using combined on- and off-shore seismic observations. *Physics of the Earth and Planetary Interiors*, *132*(1), 197–217. doi: 10.1016/S0031-9201(02)00052-3
- Contreras-Reyes, E., & Carrizo, D. (2011, May). Control of high oceanic features and subduction channel on earthquake ruptures along the Chile–Peru subduction zone. *Physics of the Earth and Planetary Interiors*, *186*(1), 49–58. doi: 10.1016/j.pepi.2011.03.002
- Cruz-Atienza, V. M., Villafuerte, C., & Bhat, H. S. (2018, July). Rapid tremor migration and pore-pressure waves in subduction zones. *Nature Communications*, *9*(1), 2900. doi: 10.1038/s41467-018-05150-3
- Danré, P., De Barros, L., Cappa, F., & Ampuero, J.-P. (2022). Prevalence of Aseismic Slip Linking Fluid Injection to Natural and Anthropogenic Seismic Swarms. *Journal of Geophysical Research: Solid Earth*, *127*(12), e2022JB025571. doi: 10.1029/2022JB025571
- Danré, P., De Barros, L., Cappa, F., & Passarelli, L. (2024, October). Parallel

- dynamics of slow slips and fluid-induced seismic swarms. *Nature Communications*, 15(1), 8943. doi: 10.1038/s41467-024-53285-3
- Delahaye, E. J., Townend, J., Reyners, M. E., & Rogers, G. (2009, January). Microseismicity but no tremor accompanying slow slip in the Hikurangi subduction zone, New Zealand. *Earth and Planetary Science Letters*, 277(1), 21–28. doi: 10.1016/j.epsl.2008.09.038
- Dublanchet, P., & De Barros, L. (2021). Dual Seismic Migration Velocities in Seismic Swarms. *Geophysical Research Letters*, 48(1), e2020GL090025. doi: 10.1029/2020GL090025
- Farge, G., Jaupart, C., Frank, W. B., & Shapiro, N. M. (2023). Along-Strike Segmentation of Seismic Tremor and Its Relationship With the Hydraulic Structure of the Subduction Fault Zone. *Journal of Geophysical Research: Solid Earth*, 128(12), e2023JB027584. doi: 10.1029/2023JB027584
- Farge, G., Jaupart, C., & Shapiro, N. M. (2021). Episodicity and Migration of Low Frequency Earthquakes Modeled With Fast Fluid Pressure Transients in the Permeable Subduction Interface. *Journal of Geophysical Research: Solid Earth*, 126(9), e2021JB021894. doi: 10.1029/2021JB021894
- Fasola, S. L., Brudzinski, M. R., Holtkamp, S. G., Graham, S. E., & Cabral-Cano, E. (2019, April). Earthquake swarms and slow slip on a sliver fault in the Mexican subduction zone. *Proceedings of the National Academy of Sciences*, 116(15), 7198–7206. doi: 10.1073/pnas.1814205116
- Gase, A. C., Bangs, N. L., Saffer, D. M., Han, S., Miller, P. K., Bell, R. E., . . . Barker, N. (2023). Subducting volcanoclastic-rich upper crust supplies fluids for shallow megathrust and slow slip. *Science Advances*, 9(33), eadh0150. Retrieved from <https://www.science.org/doi/abs/10.1126/sciadv.adh0150> doi: 10.1126/sciadv.adh0150
- Gomberg, J., Wech, A., Creager, K., Obara, K., & Agnew, D. (2016). Reconsidering earthquake scaling. *Geophysical Research Letters*, 43(12), 6243–6251. doi: 10.1002/2016GL069967
- González-Vidal, D., Moreno, M., Sippl, C., Baez, J. C., Ortega-Culaciati, F., Lange, D., . . . Heit, B. (2023). Relation Between Oceanic Plate Structure, Patterns of Interplate Locking and Microseismicity in the 1922 Atacama Seismic Gap. *Geophysical Research Letters*, 50(15), e2023GL103565. doi: 10.1029/2023GL103565
- Gosselin, J. M., Audet, P., Estève, C., McLellan, M., Mosher, S. G., & Schaeffer, A. J. (2020, January). Seismic evidence for megathrust fault-valve behavior during episodic tremor and slip. *Science Advances*, 6(4), eaay5174. doi: 10.1126/sciadv.aay5174
- Hansen, P. C., & O’Leary, D. P. (1993). The use of the l-curve in the regularization of discrete ill-posed problems. *SIAM journal on scientific computing*, 14(6), 1487–1503.
- Hayes, G. P., Moore, G. L., Portner, D. E., Hearne, M., Flamme, H., Furtney, M., & Smoczyk, G. M. (2018, October). Slab2, a comprehensive subduction zone geometry model. *Science*, 362(6410), 58–61. doi: 10.1126/science.aat4723
- Ide, S., Beroza, G. C., Shelly, D. R., & Uchide, T. (2007, May). A scaling law for slow earthquakes. *Nature*, 447(7140), 76–79. doi: 10.1038/nature05780
- Itoh, Y., Aoki, Y., & Fukuda, J. (2022, May). Imaging evolution of Cascadia slow-slip event using high-rate GPS. *Scientific Reports*, 12(1), 7179. doi: 10.1038/s41598-022-10957-8
- Itoh, Y., Socquet, A., & Radiguet, M. (2023). Largest aftershock nucleation driven by afterslip during the 2014 Iquique sequence. *Geophysical Research Letters*, 50(24), e2023GL104852.
- Kanamori, H., Rivera, L., Ye, L., Lay, T., Murotani, S., & Tsumura, K. (2019, October). New constraints on the 1922 Atacama, Chile, earthquake from historical seismograms. *Geophysical Journal International*, 219(1), 645–661. doi: 10

- .1093/gji/ggz302
- Kaneko, Y., Avouac, J.-P., & Lapusta, N. (2010). Towards inferring earthquake patterns from geodetic observations of interseismic coupling. *Nature Geoscience*, *3*(5), 363–369.
- Kato, A., & Ben-Zion, Y. (2021). The generation of large earthquakes. *Nature Reviews Earth & Environment*, *2*(1), 26–39.
- Kawano, S., Katayama, I., & Okazaki, K. (2011, October). Permeability anisotropy of serpentinite and fluid pathways in a subduction zone. *Geology*, *39*(10), 939–942. doi: 10.1130/G32173.1
- Klein, E., Duputel, Z., Zigone, D., Vigny, C., Boy, J.-P., Doubre, C., & Meneses, G. (2018). Deep Transient Slow Slip Detected by Survey GPS in the Region of Atacama, Chile. *Geophysical Research Letters*, *45*(22), 12,263–12,273. doi: 10.1029/2018GL080613
- Klein, E., Vigny, C., Duputel, Z., Zigone, D., Rivera, L., Ruiz, S., & Potin, B. (2022, December). Return of the Atacama deep Slow Slip Event: The 5-year recurrence confirmed by continuous GPS. *Physics of the Earth and Planetary Interiors*, 106970. doi: 10.1016/j.pepi.2022.106970
- Larson, K. M., Lowry, A. R., Kostoglodov, V., Hutton, W., Sánchez, O., Hudnut, K., & Suárez, G. (2004). Crustal deformation measurements in Guerrero, Mexico. *Journal of Geophysical Research: Solid Earth*, *109*(B4).
- Lavier, L. L., Tong, X., & Biemiller, J. (2021). The Mechanics of Creep, Slow Slip Events, and Earthquakes in Mixed Brittle-Ductile Fault Zones. *Journal of Geophysical Research: Solid Earth*, *126*(2), e2020JB020325. doi: 10.1029/2020JB020325
- Loverly, B., Chlieh, M., Norabuena, E., Villegas-Lanza, J., Radiguet, M., Cotte, N., ... others (2024). Heterogeneous locking and earthquake potential on the south Peru megathrust from dense GNSS network. *Journal of Geophysical Research: Solid Earth*, *129*(2), e2023JB027114.
- Maksymowicz, A., Contreras-Reyes, E., & Lara, L. E. (2024). Joint flexural-density modeling of the Taltal, Copiapó, and Iquique hotspot ridges and the surrounding oceanic plate, offshore Chile. *Geosphere*, *20*(4), 1066–1084.
- Manga, M., Beresnev, I., Brodsky, E. E., Elkhoury, J. E., Elsworth, D., Ingebritsen, S. E., ... Wang, C.-Y. (2012). Changes in permeability caused by transient stresses: Field observations, experiments, and mechanisms. *Reviews of Geophysics*, *50*(2). doi: 10.1029/2011RG000382
- Marill, L., Marsan, D., Socquet, A., Radiguet, M., Cotte, N., & Rousset, B. (2021). Fourteen-year acceleration along the Japan trench. *Journal of Geophysical Research: Solid Earth*, *126*(11), e2020JB021226.
- Marsan, D., Reverso, T., & Socquet, A. (2023, December). Earthquake swarms along the Chilean subduction zone, 2003–2020. *Geophysical Journal International*, *235*(3), 2758–2777. doi: 10.1093/gji/ggad359
- Molina, D., Tassara, A., Abarca, R., Melnick, D., & Madella, A. (2021). Frictional segmentation of the Chilean megathrust from a multivariate analysis of geophysical, geological, and geodetic data. *Journal of Geophysical Research: Solid Earth*, *126*(6), e2020JB020647.
- Molina-Ormazabal, D., Ampuero, J.-P., & Tassara, A. (2023, December). Diverse slip behaviour of velocity-weakening fault barriers. *Nature Geoscience*, *16*(12), 1200–1207. doi: 10.1038/s41561-023-01312-1
- Münchmeyer, J., Molina, D., Marsan, D., Langlais, M., Baez, J.-C., Heit, B., ... Socquet, A. (in prep). Characterising the fine-structure of the northern Chile subduction zone (24s - 31s) with > 160,000 earthquakes. *In preparation*.
- Nakajima, J., & Uchida, N. (2018, May). Repeated drainage from megathrusts during episodic slow slip. *Nature Geoscience*, *11*(5), 351–356. doi: 10.1038/s41561-018-0090-z
- Nielsen, S. (2017). *From slow to fast faulting: recent challenges in earthquake fault*

- mechanics* (Vol. 375) (No. 2103). The Royal Society Publishing.
- Nishikawa, T., & Ide, S. (2018). Recurring Slow Slip Events and Earthquake Nucleation in the Source Region of the M 7 Ibaraki-Oki Earthquakes Revealed by Earthquake Swarm and Foreshock Activity. *Journal of Geophysical Research: Solid Earth*, *123*(9), 7950–7968. doi: 10.1029/2018JB015642
- Nishikawa, T., Nishimura, T., & Okada, Y. (2021). Earthquake Swarm Detection Along the Hikurangi Trench, New Zealand: Insights Into the Relationship Between Seismicity and Slow Slip Events. *Journal of Geophysical Research: Solid Earth*, *126*(4), e2020JB020618. doi: 10.1029/2020JB020618
- Obara, K., & Kato, A. (2016, July). Connecting slow earthquakes to huge earthquakes. *Science*, *353*(6296), 253–257. doi: 10.1126/science.aaf1512
- Ojeda, J., Morales-Yáñez, C., Ducret, G., Ruiz, S., Grandin, R., Doin, M.-P., . . . Nocquet, J.-M. (2023, March). Seismic and aseismic slip during the 2006 Copiapó swarm in North-Central Chile. *Journal of South American Earth Sciences*, *123*, 104198. doi: 10.1016/j.jsames.2023.104198
- Okada, Y. (1992). Internal deformation due to shear and tensile faults in a half-space. *Bulletin of the seismological society of America*, *82*(2), 1018–1040.
- Ortega-Culaciati, F., Simons, M., Ruiz, J., Rivera, L., & Díaz-Salazar, N. (2021). An epic tikhonov regularization: Application to quasi-static fault slip inversion. *Journal of Geophysical Research: Solid Earth*, *126*(7), e2020JB021141. doi: 10.1029/2020JB021141
- Passarelli, L., Selvadurai, P. A., Rivalta, E., & Jónsson, S. (2021, August). The source scaling and seismic productivity of slow slip transients. *Science Advances*, *7*(32), eabg9718. doi: 10.1126/sciadv.abg9718
- Pastén-Araya, F., Potin, B., Azúa, K., Sáez, M., Aden-Antoniów, F., Ruiz, S., . . . Duputel, Z. (2022). Along-Dip Segmentation of the Slip Behavior and Rheology of the Copiapó Ridge Subducted in North-Central Chile. *Geophysical Research Letters*, *49*(4), e2021GL095471. doi: 10.1029/2021GL095471
- Perez-Silva, A., Kaneko, Y., Savage, M., Wallace, L., & Warren-Smith, E. (2023). Characteristics of Slow Slip Events Explained by Rate-Strengthening Faults Subject to Periodic Pore Fluid Pressure Changes. *Journal of Geophysical Research: Solid Earth*, *128*(6), e2022JB026332. doi: 10.1029/2022JB026332
- Perfettini, H., Frank, W. B., Marsan, D., & Bouchon, M. (2018). A Model of Aftershock Migration Driven by Afterslip. *Geophysical Research Letters*, *45*(5), 2283–2293. doi: 10.1002/2017GL076287
- Radiguet, M., Perfettini, H., Cotte, N., Gualandi, A., Valette, B., Kostoglodov, V., . . . Campillo, M. (2016, November). Triggering of the 2014 Mw7.3 Papanoa earthquake by a slow slip event in Guerrero, Mexico. *Nature Geoscience*, *9*(11), 829–833. doi: 10.1038/ngeo2817
- Rice, J. R., & Ben-Zion, Y. (1996). Slip complexity in earthquake fault models. *Proceedings of the National Academy of Sciences*, *93*(9), 3811–3818.
- Rolandone, F., Nocquet, J.-M., Mothes, P. A., Jarrin, P., Vallée, M., Cubas, N., . . . Font, Y. (2018, January). Areas prone to slow slip events impede earthquake rupture propagation and promote afterslip. *Science Advances*, *4*(1), eaao6596. doi: 10.1126/sciadv.aao6596
- Ruiz, S., & Madariaga, R. (2018, May). Historical and recent large megathrust earthquakes in Chile. *Tectonophysics*, *733*, 37–56. doi: 10.1016/j.tecto.2018.01.015
- Seno, T. (2003). Fractal asperities, invasion of barriers, and interplate earthquakes. *Earth, Planets and Space*, *55*(11), 649–665. doi: 10.1186/BF03352472
- Shaddock, H. R., & Schwartz, S. Y. (2019, March). Subducted seamount diverts shallow slow slip to the forearc of the northern Hikurangi subduction zone, New Zealand. *Geology*, *47*(5), 415–418. doi: 10.1130/G45810.1
- Shapiro, S. A., Patzig, R., Rothert, E., & Rindschwentner, J. (2003). Triggering of Seismicity by Pore-pressure Perturbations: Permeability-related Signatures

- of the Phenomenon. In H.-J. Kumpel (Ed.), *Thermo-Hydro-Mechanical Coupling in Fractured Rock* (pp. 1051–1066). Basel: Birkhäuser. doi: 10.1007/978-3-0348-8083-1\_16
- Singh, S. C., Hananto, N., Mukti, M., Robinson, D. P., Das, S., Chauhan, A., . . . others (2011). Aseismic zone and earthquake segmentation associated with a deep subducted seamount in sumatra. *Nature Geoscience*, 4(5), 308–311.
- Socquet, A., Tsapong-Tsague, A., Loversy, B., Janex, G., & Radiguet, M. (2023). *Metadata and GNSS daily position solutions for permanent GNSS stations in South America*. CNRS, OSUG, ISTERRE. doi: 10.17178/GNSS.products.SouthAmerica.GIPSYX.daily
- Sun, T., Saffer, D., & Ellis, S. (2020, March). Mechanical and hydrological effects of seamount subduction on megathrust stress and slip. *Nature Geoscience*, 13(3), 249–255. doi: 10.1038/s41561-020-0542-0
- Takemura, S., Hamada, Y., Okuda, H., Okada, Y., Okubo, K., Akuhara, T., . . . Tonegawa, T. (2023, October). A review of shallow slow earthquakes along the Nankai Trough. *Earth, Planets and Space*, 75(1), 164. doi: 10.1186/s40623-023-01920-6
- Tarantola, A. (2005). *Inverse problem theory and methods for model parameter estimation*. SIAM.
- Uchida, N., Inuma, T., Nadeau, R. M., Bürgmann, R., & Hino, R. (2016, January). Periodic slow slip triggers megathrust zone earthquakes in northeastern Japan. *Science*, 351(6272), 488–492. doi: 10.1126/science.aad3108
- Uchida, N., & Matsuzawa, T. (2013). Pre-and postseismic slow slip surrounding the 2011 tohoku-oki earthquake rupture. *Earth and Planetary Science Letters*, 374, 81–91.
- Vigny, C., Klein, E., & Ojeda, J. (2024, June). In search for the lost truth about the 1922 & 1918 Atacama earthquakes in Chile. *Journal of South American Earth Sciences*, 104983. doi: 10.1016/j.jsames.2024.104983
- Voss, N., Dixon, T. H., Liu, Z., Malservisi, R., Protti, M., & Schwartz, S. (2018, October). Do slow slip events trigger large and great megathrust earthquakes? *Science Advances*, 4(10), eaat8472. doi: 10.1126/sciadv.aat8472
- Wang, B., & Barbot, S. (2023, February). Pulse-like ruptures, seismic swarms, and tremorgenic slow-slip events with thermally activated friction. *Earth and Planetary Science Letters*, 603, 117983. doi: 10.1016/j.epsl.2022.117983
- Warren-Smith, E., Fry, B., Wallace, L., Chon, E., Henrys, S., Sheehan, A., . . . Lebedev, S. (2019, June). Episodic stress and fluid pressure cycling in subducting oceanic crust during slow slip. *Nature Geoscience*, 12(6), 475–481. doi: 10.1038/s41561-019-0367-x
- Yabe, S., & Ide, S. (2014). Spatial distribution of seismic energy rate of tectonic tremors in subduction zones. *Journal of Geophysical Research: Solid Earth*, 119(11), 8171–8185.
- Yáñez-Cuadra, V., Ortega-Culaciati, F., Moreno, M., Tassara, A., Krumm-Nualart, N., Ruiz, J., . . . Benavente, R. (2022). Interplate coupling and seismic potential in the atacama seismic gap (chile): Dismissing a rigid andean sliver. *Geophysical Research Letters*, 49(11), e2022GL098257. doi: 10.1029/2022GL098257

## Supplementary material

### Text S1 - GNSS data availability and processing

In this work we benefit from Chilean and international efforts to increase the density of the geodetic network monitoring the Atacama Segment. The large number of GPS stations gives high spatial resolution to capture the diversity of tectonic processes taking place. In our study, we analyse 5 permanent stations provided by the CSN and 12 temporary stations deployed by external projects. Furthermore, an additional 4 Chilean and 9 Argentinean stations are used to remove potential common noise from our data. The time window used in our analysis spans roughly 3 years, which is sufficient to recover the current interseismic loading rate. The GNSS data have been processed using GipsyX (Bertiger et al., 2020) software following a strategy described in (Loverly et al., 2024). Time series in IGS20 reference frame used in this manuscript are available at [https://doi.osug.fr/public/GNSS\\_products/GNSS.products.SouthAmerica\\_GIPSYX.daily.html](https://doi.osug.fr/public/GNSS_products/GNSS.products.SouthAmerica_GIPSYX.daily.html).

### Text S2 - GNSS data analysis

Extracting low amplitude transient deformation from GNSS time series can be challenging, specially in areas highly affected by interseismic deformation, seasonal deformation and recurrent earthquakes. In this context, one first task to be done is detecting jumps in the data related to seismic events or antenna change. To extract these steps, we fit a trajectory model in the position time series, using the ITSA package (<https://gricad-gitlab.univ-grenoble-alpes.fr/isterre-cycle/itsa>) (Marill et al., 2021). Once these contributions (jumps) have been removed from the time series, the common mode should be corrected, i.e., the temporal evolution that is common to several GNSS stations mostly due to reference frame errors (uncertainties in orbits or earth orientation parameters) or to large scale hydrological signals. To compute the common mode, we stack the detrended position time series at 13 stations located at distances above 200 km from the study area (9 stations belonging to the Argentinean Geodesy Service and 4 Chilean stations (Figure S9) in order to ensure that none of them are affected by the targeted tectonic phenomena. The common mode signal is characterized by seasonal variations on the north component, and by high frequency noise in the east and vertical components (Figure S9). The common mode is then subtracted from all GNSS position time series, decreasing the noise and highlighting more clearly the different transient signals (Figure S4).

In order to highlight the transient signal, the denoised position time series are then detrended over the 2 years preceding the SSE (09/2021 - 09/2023). In order to not be affected by the 2020-2021 deep SSE that occurred in the same area, we did not detrend using a longer time period. We obtain a new set of detrended GNSS time series with roughly zero displacement until middle August 2023 (Figure S4). Late August, several stations around the Copiapo Ridge show a slow westward (seaward) displacement. The signal is most evident in the east component, with maximum amplitude in BING and UDAT stations (Figure S4). The signal ends in early October, as shown by a flattening of the position time series.

We performed the same analysis without removing the common mode to evaluate how much the common mode analysis impacts the signal obtained for the SSE. Surprisingly, the signal displays a longer duration and increased amplitude over almost all the stations (Figure S4), most evident on the east component. We found that the common mode related to the east component depicts a strong deflection during the same period of time as the SSE (September-October 2023). To ensure that the eastern Argentinean station do not contain this transient, we performed an additional common mode estimation with only those station far north and south. Our findings show that the same

signature and pattern result in this new analysis (Figure S10). Therefore not removing the common mode pattern, would have provoked an overestimation of the SSE.

To extract the static offset displacements, we fit our data with an arctangent function. The function is similar to the one proposed by (Larson et al., 2004), parametrized by the duration  $t_d$ , the start time  $t_i$  of the SSE, and two amplitude coefficients  $a$  and  $b$ . The displacement at station  $n$  on component  $j$  is modelled as:

$$SSE_{nj}(t) = a_{nj} \arctan\left(2\pi \frac{t - t_i}{t_d}\right) + b_{nj}$$

The times  $t_d$  and  $t_i$  are fit jointly at all stations, the constants  $a$  and  $b$  independently.

### **Text S3 - Slip inversions**

To estimate the slip on the plate interface, we perform a linear least square inversion described in (Tarantola, 2005). This strategy has been adapted following (Radiguet et al., 2016). Assuming an elastic half space and a realistic slab geometry (Slab2.0 (Hayes et al., 2018)), we calculate the Green's functions (Okada, 1992). We discretize the fault into regular triangular patches of 10 km side length. We impose the slip rake in the convergence direction. We invert the surface displacements computed from the arc tangent function mentioned before. For estimating the seismic moment, we assume a shear modulus of 30 GPa. To avoid instabilities inherent to the slip inversion problem (Ortega-Culaciati et al., 2021), we set a smoothing prior on slip. For such purpose, we define the *a priori* model covariance matrix following (Radiguet et al., 2016). The covariance matrix depends on two damping constants,  $\sigma_{mo}$  and  $\lambda$ . The value of  $\sigma_{mo}$  represent the *a priori* standard deviation on fault slip. The value of  $\lambda$  represents a correlation function between neighboring fault patches, aiming to solve for a spatially smooth slip distribution. We imposed  $\lambda = 10$  km which results in a more rough solution, with low smoothing. To select an optimal regularization, we select  $\lambda$  considering the data fit  $\chi^2$  and the  $L_2$  norm of the regularized solution. Figure S11 shows the L-curves (Hansen & O'Leary, 1993) for our slip inversion.

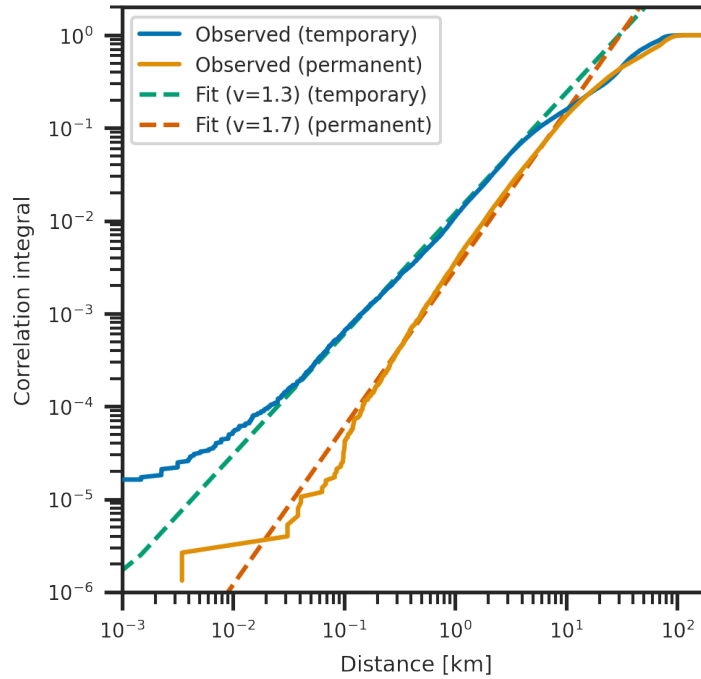


**Figure S1.** Correlation integral over distance range for the temporary and permanent catalogs. We calculate the correlation integral for all events in the boxes in Figure S8, i.e., events that occur during swarm episodes and within area of the 2023 SSE. The dashed lines show a log-log fit to determine the fractal dimension. We suspect that the higher fractal dimension for the permanent catalog is caused by the different seismicity pattern in the aftershock region of the 2020 Coquimbo earthquakes, as these events make up a large fraction of the total events in the permanent catalog in this region.

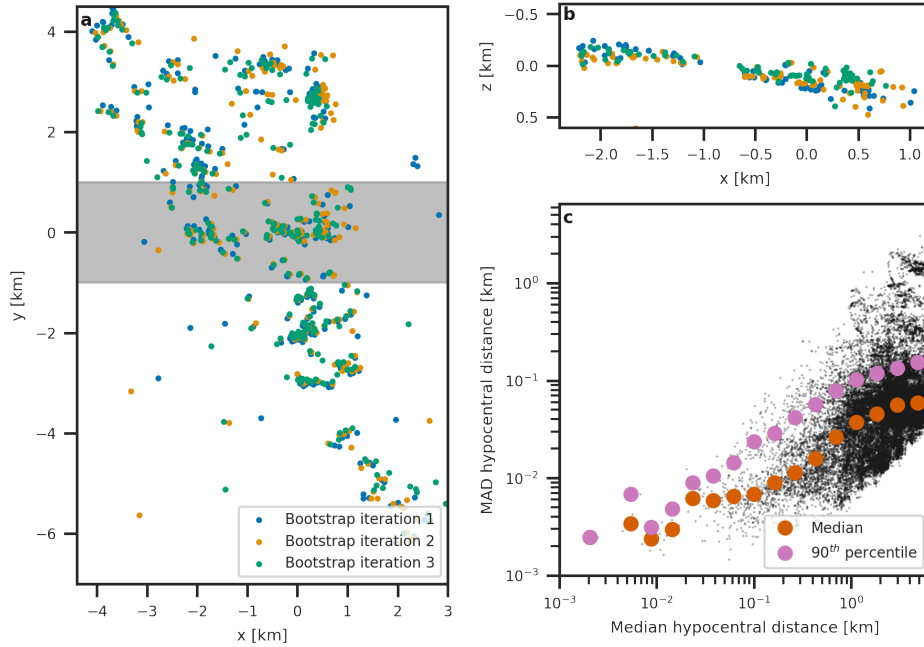


**Figure S2.** Relocation bootstrap analysis with GrowClust3D and the bootstrapping implementation of GrowClust3D. The analysis was conducted on all events located between  $72^{\circ}\text{W}$  and  $71^{\circ}\text{W}$  and between  $28^{\circ}\text{S}$  and  $26.9^{\circ}\text{S}$ . We show the initiation cluster of the 2023 SSE sequence around  $71.3^{\circ}\text{W}$   $27.3^{\circ}\text{S}$ . All events have been transformed to a local coordinate system, the absolute location offset between the individual bootstrap iterations has been removed. **a** Epicenter distribution in the first 3 bootstrap iterations. **b** Cross section through the cluster. The events shown are highlighted in grey in subplot a. **c** Statistical results from 1000 bootstrap iterations. Each black dot represents one event pair with their median hypocentral distance and the median absolute deviation of the distance as an uncertainty measure. Red and purple dots show the moving median and 90<sup>th</sup> percentile of the uncertainties.

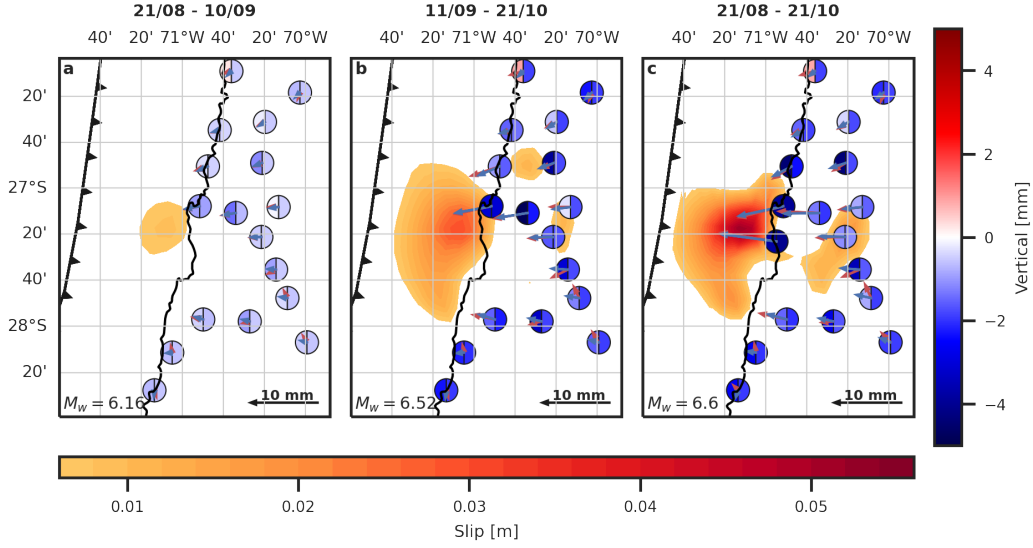


**Figure S3.** Snapshots of the slip for 3 periods. The arrows provide a comparison between observed (blue arrows) and predicted (red arrows) slip in three phases. Circles denote vertical displacement, with the left half representing the observed and the right half the predicted displacement.

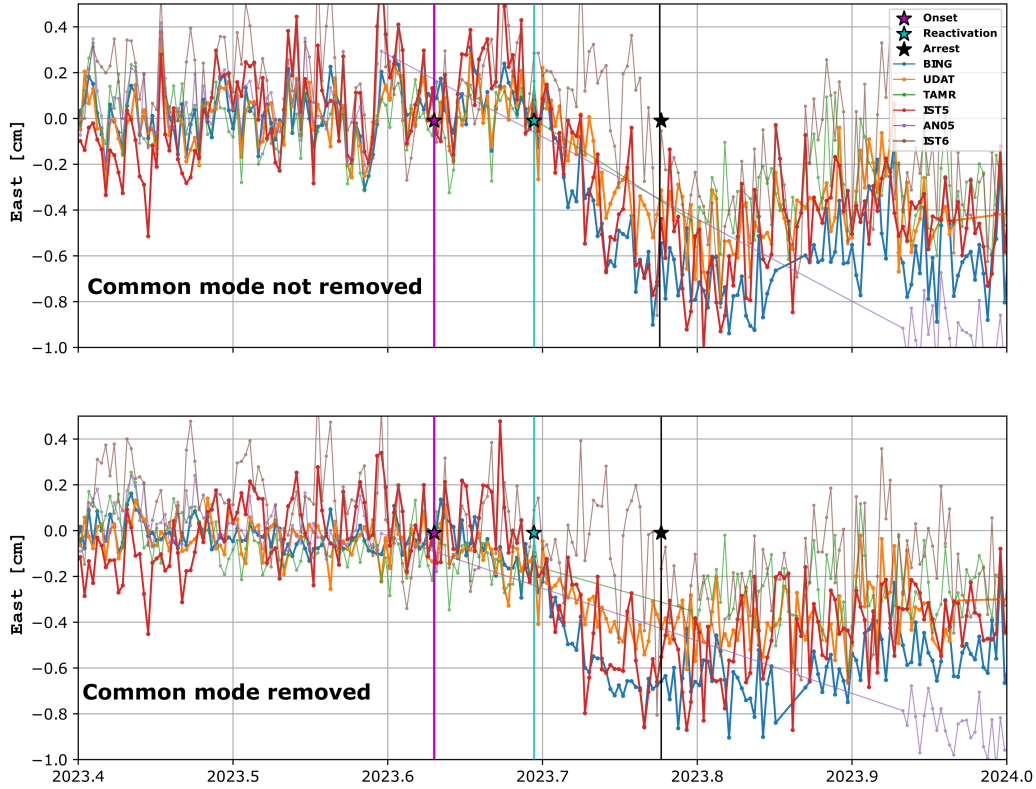


**Figure S4.** Comparison of the GNSS displacement with and without common mode removal. Top: Detrended GNSS time series before removing the common mode. Bottom: Detrended GNSS time series after removing the common mode.

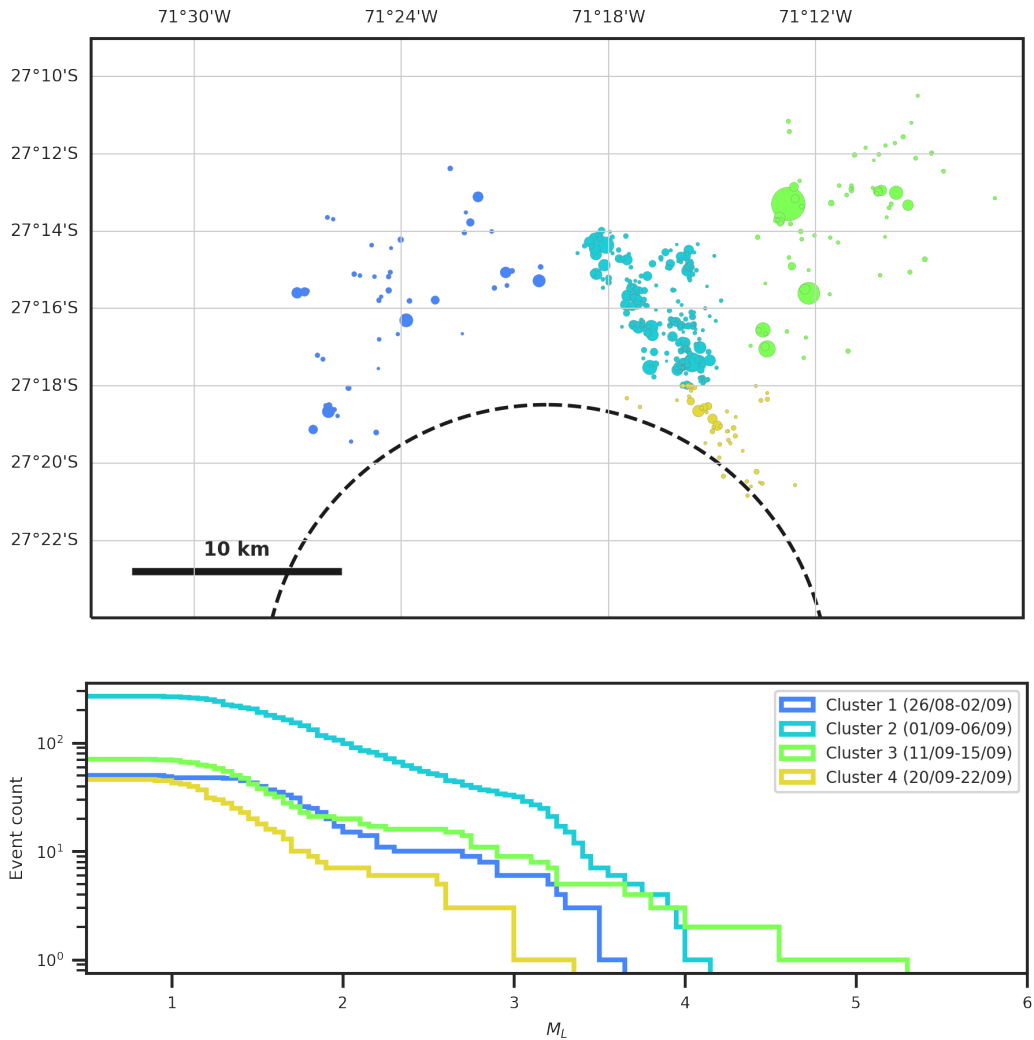


**Figure S5.** The onset sequence grouped into individual clusters with locations and magnitude distribution. The blue cluster occurs first (26/08-02/09), followed by the cyan (01/09-06/09), the green (11/09-15/09), and the yellow last (20/09-22/09). The bottom plot shows the inverse cumulative magnitude distribution. The black dashed circle indicates the approximate position of the subducted seamount inferred from bathymetry and gravity data.

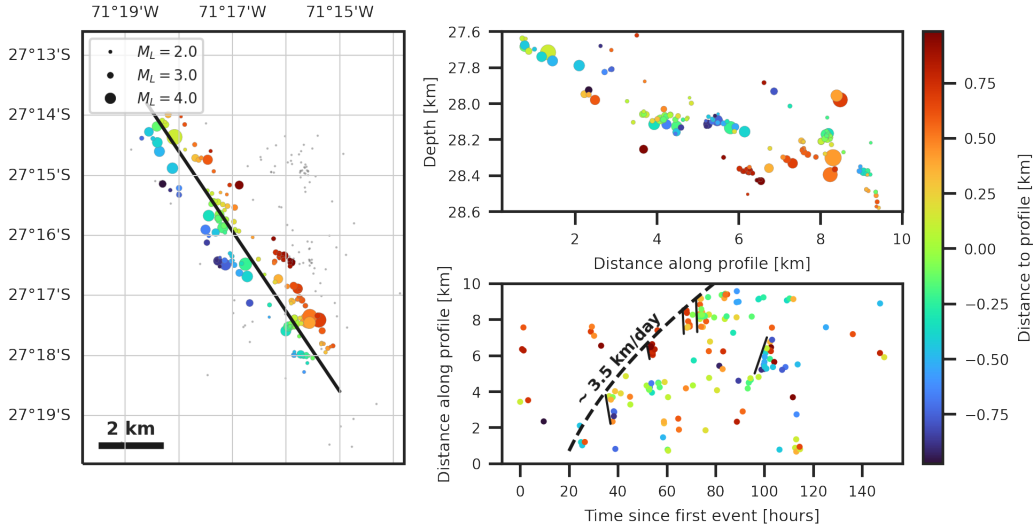


**Figure S6.** Zoom in on the highly active cluster during the onset sequence. The black line in the map plot shows the transect used in the two other plots. The transect is 2 km wide and centered around the line. All events within the transect are shown in colour on the map. We highlight the slow (dashed line) and fast (narrow, solid lines) migrations. For the fast migrations, we are not able to determine a reliable migration velocity estimate, but it is in excess of 15 km/day.

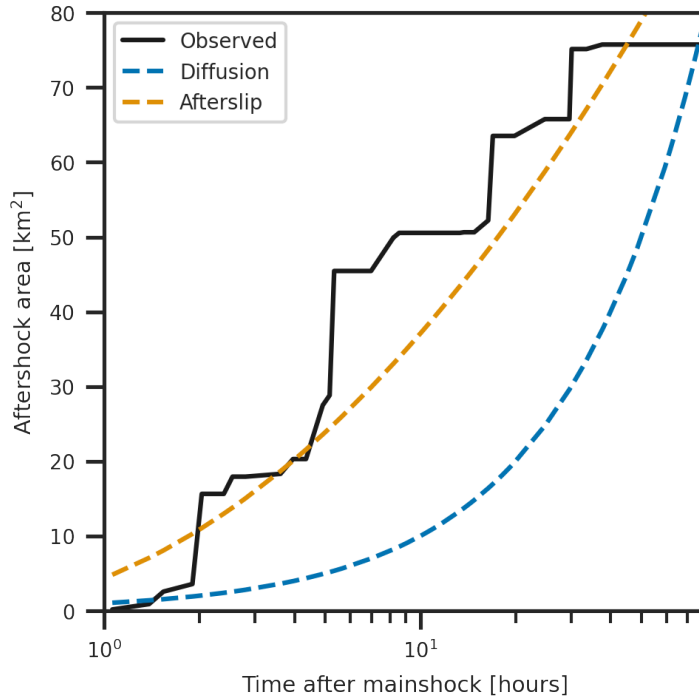


**Figure S7.** Area of the aftershocks for the  $M_L = 5.3$  event on September 11th. The area is estimated using the convex hull of all aftershocks so far. For comparison, prototypical expansion curves for afterslip (4 km per decade) (Perfettini et al., 2018) for a diffusion process ( $280 \text{ m}^2/\text{s}$ ) (Shapiro et al., 2003) have been added.

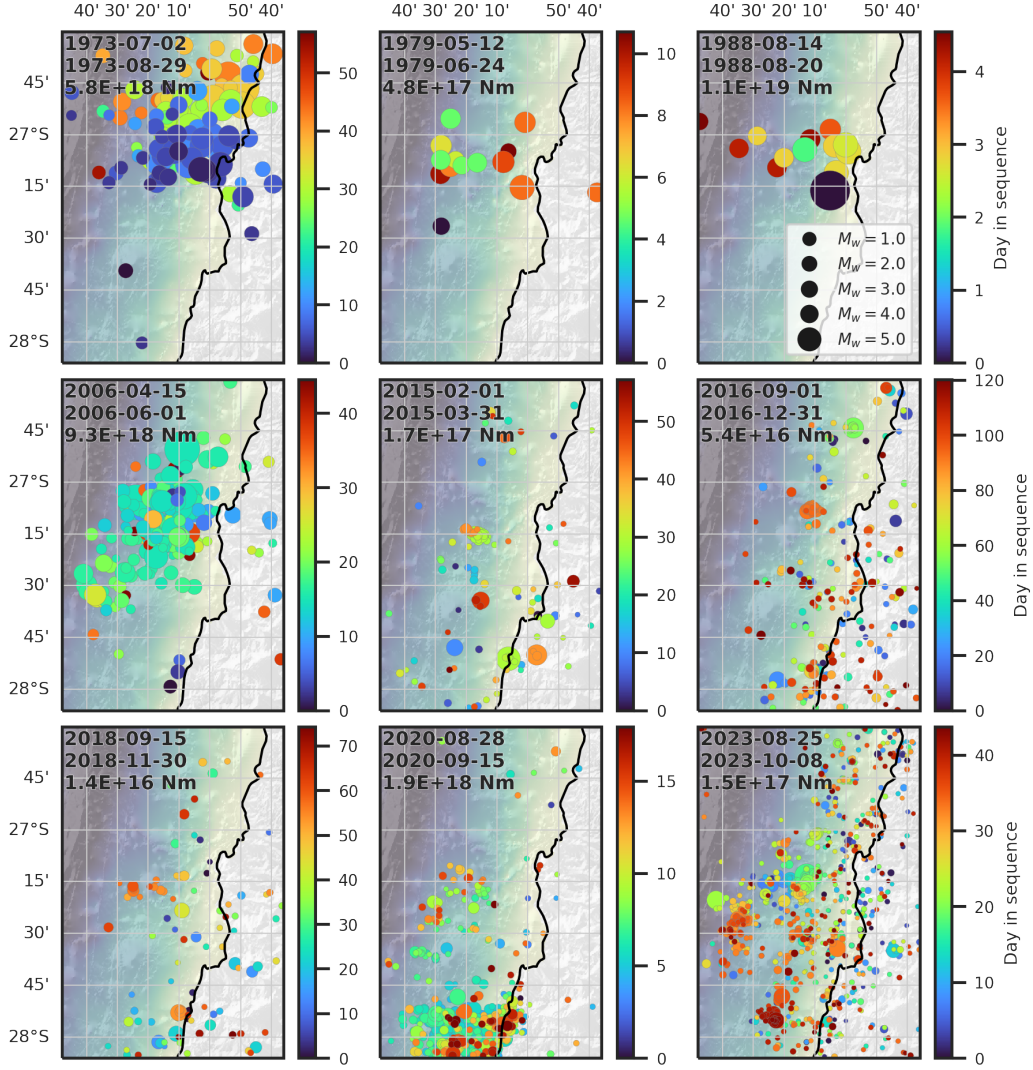


**Figure S8.** Historic records of seismic swarms and migrations in aftershock sequences. The 1973, 1979 and 1988 sequences use the USGS catalog (covering 1964 - 2024), the 2006 sequence the CSN catalog (2000 - 2024), the 2015 to 2020 sequences uses the permanent station catalog from Münchmeyer et al. (in prep) (2014 - 2024), and the 2023 sequence the temporary station catalog from Münchmeyer et al. (in prep) (11/2020 - 02/2024). The total seismic moment of all visualised events per sequence is indicated in the top left corner. A zoom in on the 2015 to 2023 swarms is available in Figure 4.

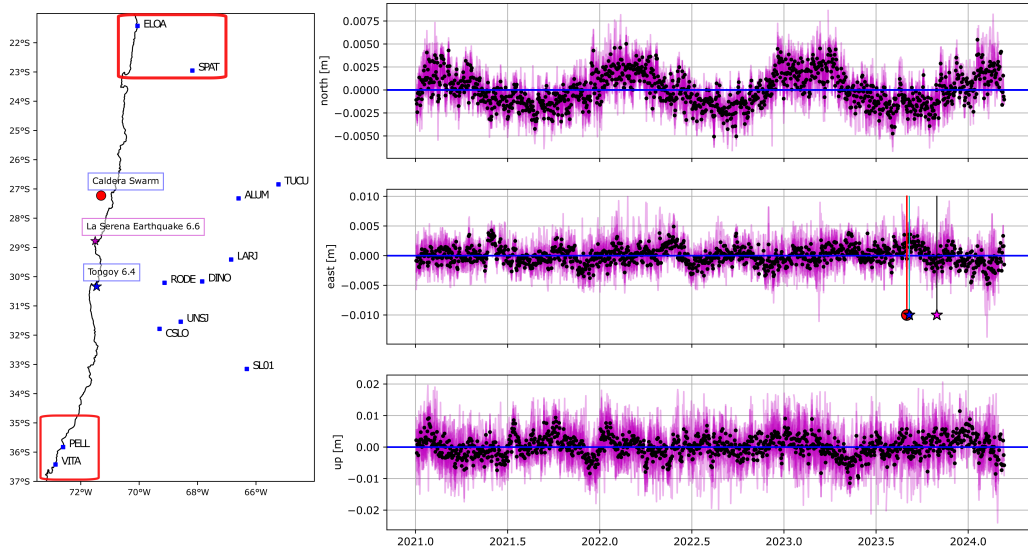


**Figure S9.** Common mode calculated from distant GNSS stations. Left: Map view GNSS stations used to compute the common mode. Red rectangles indicate the 4 Chilean GPS stations. Right: Stacked GNSS time series in pink color. Black dots depict the averaged common mode.

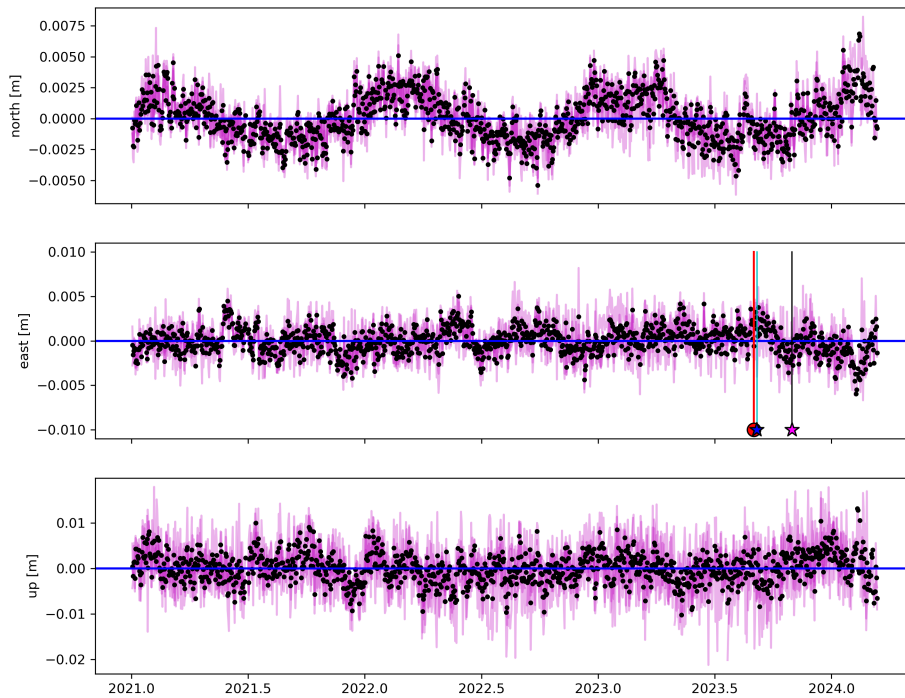


**Figure S10.** Common mode calculated from Chilean GNSS stations (Red rectangles Figure S9, Roughly 500 km from targeted area). Stacked GNSS time series in pink color. Black dots depict the averaged common mode.

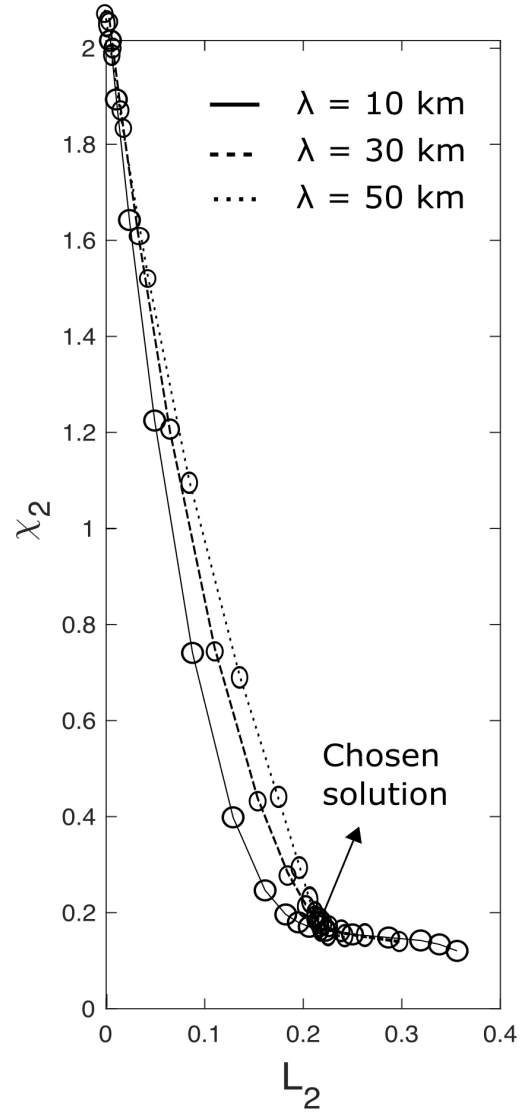


**Figure S11.** L curves criteria used in this study to select our preferred slip model.